occurs between the onset of the eclipse and its midpoint. This agrees qualitatively with the work of Allais[4] with a paraconical pendulum, where the change of azimuth increased substantially in the first half of the eclipse of 30 June 1954. Both these effects would seem to have a gravitational basis which cannot be explained by accepted classical theory.

Both our experimental findings and those of Allais cause one to question whether the classical laws of gravitation hold without modification.

CONCLUSION

Quantitative observations made with a precise torsion pendulum show, in agreement with many earlier, less precise recordings made at Harvard since 1953, that

the times required to traverse a fixed fraction of its total angular path vary markedly during the hours before the eclipse and during its first half, i.e., up to its midpoint. Also the significant changes in these times do not coincide exactly with the astronomically determined onset, midpoint, and endpoint of the eclipse.

These variations are too great to be explained, on the basis of classical gravitational theory, by the relative change in position of the moon with respect to the earth and sun. This leads to the same conclusion arrived at by Allais—that classical gravitational theory needs to be modified to interpret his (and our) experimental results. Moreover, the findings with the torsion pendulum, the significant mass of which moves perpendicularly to the geogravitic vector, seem to indicate the possibility of a fine structure in these observations neither predicted nor recorded using the orthodox methods of quasi-stationary gravitational investigations.

[4] Maurice F. C. Allais, Aerospace Eng. **18**, 46 (1959).

Symmetry, Unitarity, and Geometry in Electromagnetic Scattering*

P. C. WATERMAN

The MITRE Corporation, Bedford, Massachusetts 01730

(Received 11 August 1970)

Upon defining vector spherical partial waves $\{\psi_n\}$ as a basis, a matrix equation is derived describing scattering for general incidence on objects of arbitrary shape. With no losses present, the scattering matrix is then obtained in the symmetric, unitary form $S = -\hat{Q}'^*\hat{Q}^*$, where (perfect conductor) $\hat{Q}$ is the Schmidt orthogonalization of $Q_{nn'} = (k/\pi)\int d\sigma \cdot [(\nabla \times \mathrm{Re}\psi_n) \times \psi_{n'}]$, integration extending over the object surface. For quadric (separable) surfaces, Q itself becomes symmetric, effecting considerable simplification. A secular equation is given for constructing eigenfunctions of general objects. Finally, numerical results are presented and compared with experimental measurements.

INTRODUCTION

IN earlier work, a matrix description of acoustic scattering was given, based on the *full* Helmholtz-Kirchhoff integral formula plus interior continuation arguments.[1] The present work constitutes the sequel for the vector electromagnetic case. Close parallels between the scalar and vector formalism are evident; we have attempted to accentuate them by using the same notation whenever possible.

Section I deals with derivation of the basic equations for the transition matrix. Incident illumination is constrained only to have no singularities in the interior volume of the scatterer; both volume- and surface-type scattering are considered for objects of general geometry, the surface of which need not be smooth (i.e., have continuous-turning normal). In Sec. II the scattering matrix is defined, and symmetry and unitary constraints are introduced into the original equation to

obtain the solution in exactly symmetric, unitary form at any truncation. A secular equation is also discussed, from which one could alternatively proceed by constructing eigenfunctions appropriate to the given object. Our approach to the problem in terms of the scattering matrix in a spherical-wave basis is not new, incidentally, and has been described in some detail by Newton, for example.[2]

In Sec. III. a closer look is taken at matrix elements required in the computation. Constraints arising from the object geometry are discussed, and an important reduction found for objects bounded by quadratic surfaces, i.e., coordinate surfaces in one of the 11 systems in which the *scalar* Helmholtz equation is separable. Finally, numerical results are presented in Sec. IV for bodies with rotational symmetry, and compared with experimental measurements, as well as the Rayleigh and geometrical-optics approximations.

[1] P. C. Waterman, J. Acoust. Soc. Am. **45**, 1417 (1969).

[2] R. G. Newton, *Scattering Theory of Waves and Particles* (McGraw-Hill, New York, 1966), Chap. 2, pp. 101–104, pp. 189–190.
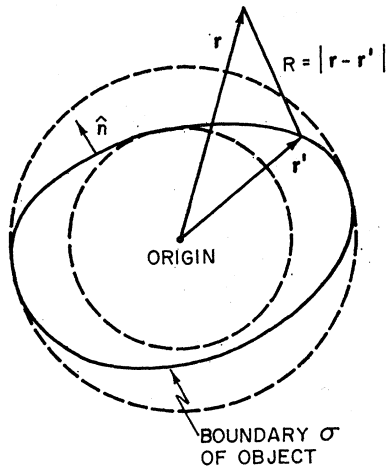
FIG. 1. Geometry of a scattering region bounded by the closed surface σ.

In other related work in the literature, numerical results have been obtained for conducting[3-7] and dielectric[8] objects. A somewhat different approach to the problem has been pursued by Mullin,[9] Greenberg,[10] and their co-workers, and, using perturbation techniques, by Yeh[11] and Erma.[12] The characteristic modes, or eigenfunctions, were considered by Garbacz.[13] The key ingredient in all of this latter work was the assumption that a representation of the scattered field in spherical (or circular cylindrical) waves may be employed directly on the surface of the object, in the course of satisfying boundary conditions. Relative merits of this assumption, versus the interior-region approach employed herein, are discussed by Bates and others.[14] Additional references to other techniques, e.g., the variational method and the surface-integral-equation formulation, have been given elsewhere.[1]

[3] N. N. Govorun, Comp. Math. Math. Phys. 1, 779 (1961).

[4] P. C. Waterman, Proc. IEEE 53, 805 (1965).

[5] R. H. T. Bates, Proc. IEE (London) 115, 1443 (1968).

[6] F. Gardner, Proc. IEEE 57, 844 (1969).

[7] A. A. Avetisyan, Radiotekn i Electron (USSR) 15, 3 (1970). [Radio Eng. Electron. (USSR) 15, 1 (1970)].

[8] P. C. Waterman, Alta Frequenza 38 (Speciale), 348 (1969).

[9] C. R. Mullin, R. Sandberg, and C. O. Velline, IEEE Trans. Antennas Propagation 13, 141 (1965).

[10] J. M. Greenberg, A. C. Lind, R. T. Wang, and L. F. Libelo in *Electromagnetic Scattering*, edited by R. L. Rowell and R. S. Stein (Gordon and Breach, New York, 1967), pp. 3–53.

[11] C. Yeh, Phys. Rev. 135, A1193 (1964); J. Math. Phys. 6, 2008 (1965).

[12] V. A. Erma, Phys. Rev. 173, 1243 (1968); 176, 1544 (1968); 179, 1238 (1969).

[13] R. J. Garbacz, Proc. IEEE 53, 856 (1965). See also V. V. Karnishin, V. V. Akindinov and V. V. Vishin, Radiotekn i Electron (USSR) 15, 14 (1970). [Radio Eng. Electron. (USSR) 15, 10 (1970)].

[14] R. H. T. Bates, IEEE Trans. Microwave Theory Techniques 15, 185 (1967); Electron. Letters 3, 166 (1967); 5, 654 (1969). M. L. Burrows, ibid. 5, 277 (1969); 5, 694 (1969). R. F. Millar, ibid. 5, 416 (1969); R. F. Millar and R. H. T. Bates, IEEE Trans. Microwave Theory Techniques 18, 325 (1970); M. Neviere, Optics Commun. 2, 51 (1970).

I. MATRIX FORMULATION

We seek the scattering from an object bounded by the closed surface σ, as shown in Fig. 1, upon illumination with a given incident electromagnetic field $\mathbf{E}^i, \mathbf{H}^i$. Only monochromatic waves are considered, with time dependence $e^{-i\omega t}$ suppressed throughout; both electric and magnetic fields satisfy the vector Helmholtz equation

$$\nabla\times\nabla\times\boldsymbol{\psi} - k^2\boldsymbol{\psi} = 0 \quad (k=\omega/c). \tag{1}$$

Defining the total field $\mathbf{E}$ as the sum of the incident and scattered waves, i.e., $\mathbf{E} = \mathbf{E}^i + \mathbf{E}^s$, and further requiring that the scattered wave be outgoing at infinity, the vector Huygen's principle states that[15]

$$\left.\begin{matrix}\mathbf{E(r)}\\0\end{matrix}\right\} = \mathbf{E}^i(\mathbf{r}) + \nabla\times\int d\sigma' k(\hat{n}\times\mathbf{E}_+)g(kR)$$

$$+\nabla\times\nabla\times\int d\sigma' i(\hat{n}\times\mathbf{H}_+)g(kR), \quad \mathbf{r}\begin{cases}\text{outside }\sigma\\\text{inside }\sigma\end{cases}. \tag{2}$$

In this equation, $R = |\mathbf{r}-\mathbf{r}'|$ is, as usual, the distance from source point to field point, $g(kR) = (4\pi kR)^{-1}e^{ikR}$ is the scalar Green's function, and the integrals represent surface distributions of magnetic and electric dipoles, respectively. The corresponding amplitudes $\hat{n}\times\mathbf{E}_+$ and $\hat{n}\times\mathbf{H}_+$ are unknowns to be determined.

In the exterior region ($\mathbf{r}$ outside σ), Eq. (2) gives a prescription for evaluating the field by quadrature of the surface currents. In the interior, on the other hand, one sees that the fields expressed by surface integrals must precisely cancel the incident wave. In order to make use of this assertion, the set of outgoing spherical-partial-wave solutions of Eq. (1) is introduced as a basis, writing[16]

$$\boldsymbol{\psi}_{n'}(\mathbf{r}) = \boldsymbol{\psi}_{\tau\sigma mn}(\mathbf{r})$$

$$\equiv \gamma_{mn}^{1/2}(k^{-1}\,\mathrm{curl})^\tau k\mathbf{r}Y_{\sigma mn}h_n(kr)$$

$$\xrightarrow[kr\gg 1]{} -\gamma_{mn}^{1/2}(-i)^{n-\tau}(1/kr)e^{ikr}\mathbf{A}_{\tau\sigma mn}(\hat{r}) \tag{3a}$$

in terms of the spherical Hankel functions of the first kind h_n. The scalar and vector spherical harmonics are defined in terms of associated Legendre functions

[15] H. Hönl, A. W. Maue, and K. Westpfahl in *Handbuch der Physik*, edited by S. Flügge, (Springer-Verlag, Berlin, 1961), Vol. 25/1, p. 240. The incident wave appears naturally in Eq. (2) in the course of working out the details of the divergence theorem. This term is absent in the Hönl, Maue, and Westpfahl result because they did not allow for sources of the total field in the exterior region.

[16] The $\boldsymbol{\psi}_{\tau=1}$ and $\boldsymbol{\psi}_{\tau=2}$ functions are, except for normalization, the $\mathbf{M}$ and $\mathbf{N}$ functions given by P. M. Morse and H. Feshbach, *Methods of Theoretical Physics* (McGraw-Hill, New York, 1953), Chaps. 11 and 13. Our vector harmonics $\mathbf{A}_{\tau=1}$ and $\mathbf{A}_{\tau=2}$ correspond similarly to the $\mathbf{C}$ and $\mathbf{B}$ functions.

$P_n{}^m$ as

$$Y_{emn}(\hat{r}) = \cos m\phi \ P_n{}^m(\cos\theta),$$

$$Y_{omn}(\hat{r}) = \sin m\phi \ P_n{}^m(\cos\theta),$$

$$\mathbf{A}_{\tau\sigma mn}(\hat{r}) = \begin{cases} \nabla\times(\mathbf{r}Y_{\sigma mn}) & (\tau=1) \\ r\nabla Y_{\sigma mn} & (\tau=2) \end{cases} \quad (3b)$$

and the normalizing constants are

$$\gamma_{mn} = \epsilon_m \frac{(2n+1)(n-m)!}{4n(n+1)(n+m)!} \quad (3c)$$

in terms of the Neumann factor $\epsilon_0 = 1$, $\epsilon_m = 2$ otherwise. The indices $\tau = 1, 2$; $\sigma = e, o$ (even, odd); $m = 0, \ldots, n$; and $n = 1, 2, \ldots$ have been collected into the single index on $\psi_{n'}$ by the scheme (the functions having $\sigma m = o0$ do not exist) $\tau\sigma mn = 1e01, 2e01, 1e11, 2e11, 1o11, \ldots$. Note the interrelations

$$\psi_{1\sigma mn} = (1/k)\nabla\times\psi_{2\sigma mn},$$

$$\psi_{2\sigma mn} = (1/k)\nabla\times\psi_{1\sigma mn}, \quad (3d)$$

which in the far field become

$$\mathbf{A}_{2\sigma mn} = \hat{r}\times\mathbf{A}_{1\sigma mn},$$

$$\mathbf{A}_{1\sigma mn} = -\hat{r}\times\mathbf{A}_{2\sigma mn}, \quad (3e)$$

exhibiting the transverse nature of the wave functions explicitly.

The ψ_n are a complete set suitable to represent the scattered wave everywhere outside of the spherical surface circumscribing the object (Fig. 1), as will be seen shortly. We also require the wave functions $\{\text{Re}\psi_n(\mathbf{r})\}$ regular at the origin, obtained by taking the real part of the ψ_n (yielding Bessel rather than Hankel function radial dependence).[16]

The incident and scattered waves are now written

$$\mathbf{E}^i(\mathbf{r}) = \sum_n a_n \ \text{Re}\psi_n(\mathbf{r}), \quad r < r_{\min \text{ on } \sigma}$$

$$\mathbf{E}^s(\mathbf{r}) = \sum_n f_n\psi_n(\mathbf{r}), \quad r > r_{\max \text{ on } \sigma} \quad (4)$$

for field points inside the inscribed sphere, or outside the circumscribed sphere, respectively, where the incident wave has been assumed to have no sources in the interior of the object.[17] Assuming linear boundary

conditions, a *transition matrix* T can be defined which computes the scattered wave from the incident wave by

$$f_n = \sum_{n'=1} T_{nn'}a_{n'}, \quad n = 1, 2, \ldots$$

or, in obvious matrix notation,

$$f = Ta. \quad (5)$$

Because the expansions of Eq. (4) may not be appropriate to use directly in satisfying boundary conditions, we shall instead proceed by enforcing Eq. (2) in the interior region ($\mathbf{r}$ inside σ). One first rewrites the integrand in the form

$$(\hat{n}\times\mathbf{E}_+)g(kR) = (\hat{n}\times\mathbf{E}_+)\cdot\Im g(kR)$$

(and similarly for the second integral), and observes that the free-space Green's dyad may be written[16]

$$\Im g(kR) = (i/\pi)\sum \psi_n(\mathbf{r}_>) \ \text{Re}\psi_n(\mathbf{r}_<)$$
$$+ (\text{irrotational terms}). \quad (6)$$

This expansion is uniformly convergent for $r \neq r'$, with $r_>, r_<$ respectively the greater and lesser of r, r'.

Substituting Eq. (6) in Eq. (2) and performing the indicated curl operations (which eliminate the irrotational terms), the scattered wave in the exterior region is found precisely in the form given by Eq. (4), with expansion coefficients

$$f_n = \frac{k^2}{\pi}\int d\sigma\{(ik)^{-1}[\nabla\times\text{Re}(\psi_n)]\cdot(\hat{n}\times\mathbf{E}_+)$$

$$- \text{Re}(\psi_n)\cdot(\hat{n}\times\mathbf{H}_+)\}, \quad n = 1, 2, \ldots. \quad (7a)$$

On the other hand, for field points inside the inscribed sphere, the entire right-hand side of Eq. (2) takes the form of an expansion in the regular functions $\text{Re}\psi_n$. Because of orthogonality, each coefficient must vanish separately, giving

$$a_n = -\frac{k^2}{\pi}\int d\sigma[(ik)^{-1}(\nabla\times\psi_n)\cdot(\hat{n}\times\mathbf{E}_+)$$

$$- \psi_n\cdot(\hat{n}\times\mathbf{H}_+)], \quad n = 1, 2, \ldots. \quad (7b)$$

These last equations are necessary and sufficient conditions for satisfaction of Eq. (2) within the inscribed sphere. Because of the continuation property of solutions of elliptic partial differential equations, it follows that Eq. (2) will in actuality be satisfied throughout the interior of the object.[18] Equations (7) correspond, in more compact notation, to the moment equations given previously for conducting[4] and dielec-

---

[17] We have indicated in Eqs. (4) the *smallest* region in each case for which convergence of the spherical wave expansion is assured, based essentially on Eq. (6). In specific cases convergence may obtain over a larger region. For example, the inscribed sphere shown in Fig. 1 is appropriate for an incident wave consisting of a point electric dipole just outside the surface of the object, whereas the incident *plane-wave* expansion is known to converge over the entire space. For the scattered wave, which is physically well-defined everywhere outside the object, there is no guarantee that our *representation* of it in Eq. (4) will converge, and hence be useful, in the annular volume between the object surface and the circumscribing sphere. This is precisely the point discussed in Ref. 14. Further pertinent discussions are also given by V. H. Weston and W. M. Boerner, Can. J. Phys. **47**, 1177 (1969); and R. Mittra and D. R. Wilton, Proc. IEEE **57**, 2064 (1969).

[18] The field we are dealing with is a solution of Eq. (1) with no singularities anywhere in the interior volume. It may hence be reexpanded in the functions $\text{Re}\psi_n$ about a new origin within the inscribed sphere and shown to vanish within a new inscribed sphere. By repetition of this process one can eventually cover the entire interior volume.

tric[8] bodies. The first set, Eqs. (7a), constitute a quadrature rule for obtaining the scattering from surface fields, while Eqs. (7b) represent *one* equation for the *two* unknown surface fields. A second equation must be obtained from the boundary conditions, now to be specified.

The simplest case arises when the object is perfectly conducting, whereupon

$$\hat{n} \times \mathbf{E}_+(\mathbf{r}) = 0, \quad \mathbf{r} \text{ on } \sigma. \tag{8}$$

In this event we choose to represent the induced electric surface current $\hat{n} \times \mathbf{H}_+$ by expansion in regular wave functions, writing

$$\hat{n} \times \mathbf{H}_+(\mathbf{r}) = -(1/ik) \sum \alpha_n \hat{n} \times [\nabla \times \text{Re}\psi_n(\mathbf{r})], \quad \mathbf{r} \text{ on } \sigma. \tag{9}$$

These functions are a complete set, and the expansion of Eq. (9) approximates the surface current in mean-square sense.[19] Introducing the matrix Q with elements

$$Q_{nn'} = \frac{k}{\pi} \int d\boldsymbol{\sigma} \cdot [(\nabla \times \text{Re}\psi_n) \times \psi_{n'}], \tag{10}$$

the result of substituting Eq. (8) and (9) in Eqs. (7) may be written (Q' designates the transpose of Q)

$$f = -i \, \text{Re}(Q')\alpha, \tag{11a}$$

$$a = iQ'\alpha. \tag{11b}$$

The latter equation may be solved for the surface currents (α) in terms of the incident field (a), the first equation then yielding the scattered wave (f). Alternatively, the surface currents may be eliminated to get the scattered wave directly; i.e., $f = -\text{Re}(Q')(Q')^{-1}a$. Now by comparison with Eq. (5), the transition matrix is seen to be determined by (assuming T symmetric; see below)

$$QT = -\text{Re}Q. \tag{12}$$

Equation (12) applies also to the general case of an object with relative dielectric constant ϵ, relative permeability μ, and conductivity σ, after appropriate modification of Q. Boundary conditions now require continuity of the tangential components of both $\mathbf{E}$ and $\mathbf{H}$, i.e.,

$$\left. \begin{array}{l} \hat{n} \times \mathbf{E}_+ = \hat{n} \times \mathbf{E}_- \\ \hat{n} \times \mathbf{H}_+ = \hat{n} \times \mathbf{H}_- \end{array} \right\}, \quad \mathbf{r} \text{ on } \sigma. \tag{13}$$

We suppose the field inside the object to be representable in regular wave functions of the *interior* wave

equation, writing[20]

$$\mathbf{E}(\mathbf{r}) = \sum \alpha_n \, \text{Re}\psi_n(k'\mathbf{r}), \quad \mathbf{r} \text{ inside } \sigma \tag{14}$$

with interior propagation constant $k' = (k^2\mu\epsilon + i\omega\mu\mu_0\sigma)^{1/2}$. In view of the relation $\mathbf{H} = (ik\mu)^{-1}\nabla \times \mathbf{E}$ and the boundary condition Eqs. (13), both surface fields appearing in Eqs. (7) are expressible in terms of the expansion coefficients α.[21] Consequently Eqs. (11) and (12) again apply, provided Q is replaced by the matrix $\bar{Q}$ with elements

$$\bar{Q}_{nn'} = \frac{k}{\pi} \int d\boldsymbol{\sigma} \cdot \{ (1/\mu)[\nabla \times \text{Re}\psi_n(k'\mathbf{r})] \times \psi_{n'}(k\mathbf{r}) - \text{Re}\psi_n(k'\mathbf{r}) \times [\nabla \times \psi_{n'}(k\mathbf{r})] \}. \tag{15}$$

Note that the perfectly conducting object could be regarded as a limiting case of Eq. (15), obtained by setting $\sigma = 0$, $\mu = 1/\epsilon$ (so that $k' = k$), then letting $\epsilon \to \infty$, whereupon $\mu\bar{Q} \to Q$.

Far-field behavior is conveniently described by introducing the column array $\mathbf{a}(\hat{k})$ having components

$$\mathbf{a}_{n'}(\hat{k}) = (i)^{n-\tau+1}\gamma_{mn}^{1/2}\mathbf{A}_{\tau\sigma mn}(\hat{k}). \tag{16}$$

Now from Eqs. (3a), (4), and (5), the scattered wave becomes asymptotically

$$\mathbf{E}^s(\mathbf{r}) \to (e^{ikr}/ikr)\mathbf{a}'^*(\hat{k})Ta. \tag{17}$$

In particular, for plane-wave incidence in the direction $\hat{k}_i$, one can write[16]

$$\mathbf{E}^i(\mathbf{r}) = \hat{e}_0 e^{i\mathbf{k}_i \cdot \mathbf{r}} = 4\hat{e}_0 \cdot \mathbf{a}'(\hat{k}_i) \, \text{Re}(\psi), \tag{18}$$

where $\text{Re}(\psi)$ represents the column array with entries $\text{Re}(\psi_{n'})$. It follows from this last equation, incidentally, that $\mathbf{a}(-\hat{k}) = \mathbf{a}^*(\hat{k})$. Equation (17) may now be written

$$\mathbf{E}^s(\mathbf{r}) \to (e^{ikr}/r)\mathfrak{F}(\mathbf{k},\mathbf{k}_i) \cdot \hat{e}_0, \tag{19a}$$

$$\mathfrak{F}(\mathbf{k},\mathbf{k}_i) = (4/ik)\mathbf{a}'^*(\hat{k})Ta(\hat{k}_i). \tag{19b}$$

The dyadic amplitude $\mathfrak{F}$ is convenient in that it allows one to discuss properties of the scattered field without specifying polarization states involved, e.g., the linear polarization of Eq. (18). General properties have been given by Saxon[22]:

$$\mathbf{k} \cdot \mathfrak{F}(\mathbf{k},\mathbf{k}_i) = \mathfrak{F}(\mathbf{k},\mathbf{k}_i) \cdot \mathbf{k}_i = 0, \tag{20a}$$

$$\mathfrak{F}(\mathbf{k},\mathbf{k}_i) = \mathfrak{F}'(-\mathbf{k}_i, -\mathbf{k}), \tag{20b}$$

$$\int d\Omega \, \mathfrak{F}'^*(\mathbf{k},\mathbf{k}_i) \cdot \mathfrak{F}(\mathbf{k},\mathbf{k}_i') + (4\pi^2/k^2)\mathfrak{K}(\mathbf{k}_i,\mathbf{k}_i')$$
$$= (2\pi/ik)[\mathfrak{F}(\mathbf{k}_i,\mathbf{k}_i') - \mathfrak{F}'^*(\mathbf{k}_i',\mathbf{k}_i)], \tag{20c}$$

[19] The functions of Eq. (9) are a complete set for the representation of tangential vector fields over the surface σ, except at those discrete eigenvalues of k corresponding to resonance frequencies of the interior region. Proof is exactly analogous to that given in the acoustic case (Ref. 1), and will not be repeated here. Note that previous work for conducting objects (Ref. 3) employed *outgoing* rather than *regular* wave functions to represent surface currents.

[20] The case of nonzero conductivity (k' complex) is included without introducing additional notation, by agreeing to read $\text{Re}\psi_n$ as the "regular part of ψ_n," meaning to take only the Bessel-function portion (of complex argument) of the Hankel function. For k' real this definition reduces correctly to the real part of ψ_n.

[21] As noted earlier for dielectrics (Ref. 8) it is not necessary to assume that the expansion of Eq. (14) (and its curl) converge throughout the interior of σ. One can alternatively begin with $\hat{n} \times \mathbf{E}_-$ derived from Eq. (14), and the independent expansion $\mathbf{H} = \sum \beta_n \nabla \times \text{Re}\psi_n(k'r)$ to describe $\hat{n} \times \mathbf{H}_-$. By reformulating Eq. (2) through application of the divergence theorem to the interior region, it will then follow that $\beta_n \equiv \alpha_n$.

[22] D. S. Saxon, Phys. Rev. 100, 1771 (1955); see also Ref. 2.

where $\mathfrak{K}$ is a dyadic characterizing dissipation due to the obstacle. The first of these, transversality, is satisfied for our representation, Eq. (19b), by inspection. The reciprocity condition (20b) is met provided T is symmetric, i.e.,

$$T' = T. \tag{21a}$$

Finally, in the absence of any losses associated with the obstacle, Eq. (20c) requires that

$$T'^*T = -\text{Re}T. \tag{21b}$$

In the quantum theory of scattering, this equation is known as the generalized *optical theorem.*[2]

The absorption, scattering, and extinction cross sections $(\sigma_e = \sigma_a + \sigma_s)$ for the incident wave of Eq. (18) are given respectively by[22]

$$\sigma_a = (4\pi^2/k^2)\hat{e}_0 \cdot \mathfrak{K}(\mathbf{k}_i, \mathbf{k}_i) \cdot \hat{e}_0, \tag{22a}$$

$$\sigma_s = \int d\Omega \; \hat{e}_0 \cdot \mathfrak{F}'^*(\mathbf{k}, \mathbf{k}_i) \cdot \mathfrak{F}(\mathbf{k}, \mathbf{k}_i) \cdot \hat{e}_0$$

$$= (16\pi/k^2)\hat{e}_0 \cdot \mathbf{a}'^*(\hat{k}_i)T'^*T\mathbf{a}(\hat{k}_i) \cdot \hat{e}_0, \tag{22b}$$

$$\sigma_e = (4\pi/k) \; \text{Im}[\hat{e}_0 \cdot \mathfrak{F}(\mathbf{k}_i, \mathbf{k}_i) \cdot \hat{e}_0]$$

$$= -(16\pi/k^2)\hat{e}_0 \cdot \mathbf{a}'^*(\hat{k}_i) \; \text{Re}(T)\mathbf{a}(\hat{k}_i) \cdot \hat{e}_0. \tag{22c}$$

The back-scattering or radar cross section, which is the quantity most accessible to experimental measurement, is given by

$$\sigma_b = 4\pi \; | \hat{e}_0 \cdot \mathfrak{F}(-\mathbf{k}_i, \mathbf{k}_i) \cdot \hat{e}_0 |^2$$

$$= (64\pi/k^2) | \hat{e}_0 \cdot \mathbf{a}'(\hat{k}_i)T\mathbf{a}(\hat{k}_i) \cdot \hat{e}_0 |^2. \tag{22d}$$

For the orthogonally polarized return, σ_b is obtained by replacing one factor $\hat{e}_0$ by $\hat{k}_i \times \hat{e}_0$.

II. ROLE OF RECIPROCITY AND ENERGY CONSERVATION

The matrix Eq. (12) can be solved numerically after truncation, as will be shown. In the event that there are no losses associated with the obstacle, however, a more powerful procedure is available, consisting basically of solving Eq. (12) subject to constraints of symmetry and unitarity.

To begin with, one defines the scattering matrix S as

$$S = 1 + 2T. \tag{23}$$

Note that T describes the total field in terms of incident and scattered waves, i.e.,

$$\mathbf{E} = \mathbf{a}' \; \text{Re}(\psi) + \mathbf{a}'T\psi. \tag{24a}$$

In terms of the scattering matrix, the field is alternatively decomposed into *incoming* and *outgoing* waves to get

$$\mathbf{E} = \frac{1}{2}(\mathbf{a}'\psi^* + \mathbf{a}'S\psi). \tag{24b}$$

By substitution of the definition Eq. (23) in Eqs. (12), (21a) and (21b), S is seen to satisfy

$$QS = -Q^*, \tag{25a}$$

subject also to the constraints

$$S' = S, \tag{25b}$$

$$S'^*S = 1 \tag{25c}$$

of symmetry and unitarity.[23]

Now notice that if S could be constructed in the form $U'U$, where U is unitary, then both constraints would be satisfied by inspection. This suggests that Eq. (25a) be solved by first associating Q with some unitary matrix $\hat{Q}$. This can be done (in truncation) by Schmidt orthogonalization on the row vectors of Q, starting at the bottom. In matrix form one has simply

$$\hat{Q} = MQ, \tag{26}$$

with M upper-triangular. The last (and only nonzero) entry in the bottom row of M normalizes the last row vector of Q to unit length, the two elements of the next-to-bottom row of M choose a (normalized) linear combination of the next-to-last and last vector of Q orthogonal to the latter, and so on. We also agree to choose the diagonal elements of M to be real in the course of this process, which can be done without difficulty.

Premultiplying Eq. (25a) by M, one has

$$\hat{Q}S = -MQ^* = -MM^{*-1}\hat{Q}^*,$$

and hence

$$S = -\hat{Q}'^*(MM^{*-1})\hat{Q}^*. \tag{27}$$

Because M is upper-triangular with real diagonal elements, it is easy to show that the product MM^{*-1} is unit upper-triangular (i.e., all diagonal elements equal 1). Furthermore, in the limiting case of infinite matrix size, symmetry of S applies, and this in turn requires that MM^{*-1} be symmetric, as readily seen from Eq. (27). But then MM^{*-1} can only be the identity matrix (that is to say, M is real). Using this limit in the truncated Eqs. (27) gives a new sequence of truncated solutions

$$S = -\hat{Q}'^*\hat{Q}^* \quad (\text{or } T = -\hat{Q}'^* \; \text{Re}\hat{Q}) \tag{28}$$

which might be expected to converge more rapidly than Eq. (27), because symmetry and unitarity are now satisfied at each truncation. Numerical results strongly bear this out.

It may alternatively be profitable to view Eqs. (25) as an eigenvalue problem. Although this approach has not been pursued in detail, it is worth noting that in consequence we can define eigenfunctions of the

---

[23] The additional condition $SS'^* = 1$, which is required for unitarity of infinite matrices, now follows from Eqs. (25b) and (25c). Concerning this point, see also Ref. 22.

conducting ellipsoid, prolate spheroid, and oblate spheroid, all cases for which standard separation-of-variables techniques fail.[16]

The eigenvectors $u^{(j)}$ of the scattering matrix are defined by

$$S u^{(j)} = e^{i\lambda_j} u^{(j)}, \quad j = 1, 2, \ldots. \qquad (29a)$$

The eigenvalues $e^{i\lambda_j}$ lie on the unit circle in the complex plane, and the $u^{(j)}$ form a *real*, orthonormal set.[1,13] Substitution in Eq. (25a) thus leads to a real system of equations

$$\mathrm{Re}(Q) u^{(j)} = \tan(\tfrac{1}{2}\lambda_j)\,\mathrm{Im}(Q) u^{(j)} \qquad (29b)$$

for the $u^{(j)}$, after solving the secular equation

$$|\mathrm{Re}Q - \tan(\tfrac{1}{2}\lambda_j)\,\mathrm{Im}Q| = 0 \qquad (29c)$$

for the eigenvalues. The outgoing eigenfunctions are finally defined as

$$\phi_j(\mathbf{r}) \equiv \sum u_n^{(j)} \psi_n(\mathbf{r}). \qquad (29d)$$

In particular for spheroids and ellipsoids, Q is symmetric (see Sec. III), and consequently $\mathrm{Re}Q$ and $\mathrm{Im}Q$ commute[1] and must have common eigenvectors. It may then be simpler to replace Eq. (29b) by either

$$\mathrm{Re}(Q) u^{(j)} = \alpha_j u^{(j)} \qquad (29b')$$

or

$$\mathrm{Im}(Q) u^{(j)} = \beta_j u^{(j)}, \qquad (29b'')$$

where

$$\alpha_j/\beta_j = \tan\lambda_j.$$

In the acoustic case, eigenfunctions defined in the manner of Eq. (29d) have been identified numerically in one instance as expansions of the Mathieu functions (separation of variables) in circular wave functions.[1]

III. STRUCTURE OF Q MATRIX

Using Green's second vector identity,[24] the Q matrix for conducting bodies may be rewritten in the somewhat more symmetric form

$$Q_{nn'} = \tfrac{1}{2}i\delta_{nn'} + \frac{k}{2\pi} \int d\boldsymbol{\sigma} \cdot [(\nabla \times \mathrm{Re}\psi_n) \times \psi_{n'} \\ - \mathrm{Re}\psi_n \times (\nabla \times \psi_{n'})]. \qquad (10')$$

By inspection the real part of Q is seen to be symmetric, i.e.,

$$\mathrm{Re}Q_{\tau\sigma m n\tau'\sigma' m' n'} = \mathrm{Re}Q_{\tau'\sigma' m' n'\tau\sigma m n}. \qquad (30a)$$

Because the curl operation is equivalent to switching the value of τ [see Eq. (3d)], we have also that

$$Q_{2\sigma m n 2\sigma' m' n'} = \tfrac{1}{2}i\delta_{\sigma\sigma'}\delta_{mm'}\delta_{nn'} - Q_{1\sigma m n 1\sigma' m' n'}, \qquad (30b)$$

$$Q_{1\sigma m n 2\sigma' m' n'} = -Q_{2\sigma m n 1\sigma' m' n'}, \qquad (30c)$$

and

$$\mathrm{Re}Q_{\tau\sigma m n\tau'\sigma m n} = 0, \quad \tau \neq \tau'. \qquad (30d)$$

Finally, from the Wronskian relation $(x = kr)$

$$ix^2[j_n(x)h_{n+1}(x) - j_{n+1}(x)h_n(x)] = 1$$

and inspection of the angular integrations in Eq. (31b) below, one has

$$Q_{\tau\sigma m n\tau'\sigma' m'(n+1)} = Q_{\tau\sigma' m'(n+1)\tau'\sigma m n}, \quad \tau \neq \tau'. \qquad (30e)$$

These equations reduce the number of elements to be evaluated to about three-eighths of the original, and also provide useful consistency checks on numerical calculations.

Further reductions may occur depending on the object geometry. Defining scalar wave functions

$$\chi_{n'}(\mathbf{r}) = \gamma_{mn}^{1/2} Y_{\sigma m n}(\hat{r}) h_n(kr),$$

the independent elements of Q in view of Eqs. (30b) and (30c) may be written[25]

$$Q_{nn'} = \tfrac{1}{2}i\delta_{nn'} + \frac{k}{2\pi} \int d\boldsymbol{\sigma} \\ \cdot \{\nabla[(r\,\mathrm{Re}\chi_n)_r(r\chi_{n'})_r - (kr)^2\,\mathrm{Re}(\chi_n)\chi_{n'}] \\ + 2\hat{r}\hat{r}\cdot\nabla[(kr)^2\,\mathrm{Re}(\chi_n)\chi_{n'}]\}, \quad \tau = \tau' = 1 \qquad (31a)$$

$$Q_{nn'} = \frac{k^2}{\pi} \int d\boldsymbol{\sigma}\cdot\hat{r}\hat{r}\cdot[\nabla(r\,\mathrm{Re}\chi_n)\times\nabla(r\chi_{n'})], \\ \tau = 1, \tau' = 2. \qquad (31b)$$

In these equations $d\boldsymbol{\sigma} = r^2\sin\theta d\theta d\phi(\hat{r} - \hat{\theta}r_\theta/r - \hat{\phi}r_\phi/r\sin\theta)$, subscripts denote partial derivatives, $\nabla = \hat{r}\partial/\partial r + \hat{\theta}\partial/r\partial\theta + \hat{\phi}\partial/r\sin\theta\partial\phi$, and r is set equal to $r(\theta,\phi)$, defining the object surface, *after* the gradient operations are performed. Now, if there is mirror symmetry across the $x = 0$ plane $(\phi = 0, \pi)$, then by inspection

$$Q = 0, \quad (\tau + \tau' + \sigma + \sigma') \text{ odd}. \qquad (32a)$$

Similarly for mirror symmetry across $y = 0$ $(\phi = \tfrac{1}{2}\pi, \tfrac{3}{2}\pi)$,

$$Q = 0, \quad (\tau + \tau' + \sigma + \sigma' + m + m') \text{ odd} \qquad (32b)$$

and for the symmetry plane $z = 0$ $(\theta = \tfrac{1}{2}\pi)$,

$$Q = 0, \quad (\tau + \tau' + m + m' + n + n') \text{ odd}. \qquad (32c)$$

The order-of-magnitude behavior of elements of Q is governed by the radial functions. For a given argument x, the Bessel functions $j_n(x)$ decrease rapidly in magnitude, and the Neumann functions $n_n(x)$ increase, roughly as soon as index n exceeds x. Thus the real part of Q will eventually decrease rapidly in magnitude as one proceeds out along any row or column. For the imaginary part of Q, on the other hand, elements again eventually decrease going down any column, but

[24] J. A. Stratton, *Electromagnetic Theory* (McGraw-Hill, New York, 1941), p. 250.

[25] The first of these forms is obtained from Eq. (10') by writing $(1/k)\nabla\times\psi_{1\sigma m n} = \psi_{2\sigma m n} = \hat{r}(kr)\chi_{\sigma m n} + (1/k)\nabla(r\chi_{\sigma m n})_r$, and similarly for $\nabla\times\mathrm{Re}\psi_{1\sigma m n}$, then applying Stokes' theorem to the terms containing the gradient. The second form follows from $\psi_{1\sigma m n} = \nabla(r\chi_{\sigma m n})\times\hat{r}$ and the vector identity $(\mathbf{a}\times\mathbf{c})\times(\mathbf{b}\times\mathbf{c}) = \mathbf{c}\mathbf{c}\cdot(\mathbf{a}\times\mathbf{b})$.

increase going out any row. Normalization is such that diagonal elements remain of order unity.

The numerically dominant parts of the leading terms above the diagonal in $\text{Im}Q$ vanish upon integration, however. For n, n' sufficiently large, and $n'>n$—in the Rayleigh limit *all* terms above the diagonal—the leading contribution (i.e., the lowest power of kr) comes from the first term in the integrand of Eq. (31a), and is proportional to the gradient of

$$(kr)^{n-n'-1}Y_{\sigma mn}(\hat{r})Y_{\sigma' m'n'}(\hat{r}) .$$

The product of spherical harmonics can be expanded in the form[26]

$$Y_{\sigma mn}(\hat{r})Y_{\sigma' m'n'}(\hat{r}) \doteq \sum Y_{\sigma''m''n''}(\hat{r}) \qquad (33)$$

with $(\sigma+\sigma'+\sigma'')$ even, $m''=|m'\pm m|$, and $n'-n\leq n'' \leq n'+n$, $(n+n'+n'')$ even. Now the leading term in Eq. (33), i.e., $Y_{\sigma''m''(n'-n)}$, would normally make the largest contribution to Q because of undergoing fewer oscillations in the course of integration. But using the term in question, Eq. (31a) then calls for the integral of the normal gradient of a potential function, and consequently vanishes identically. This effect may significantly improve the convergence of our solutions for general bodies.

If the object is bounded by a quadric surface, i.e., a coordinate surface for which the *scalar* Helmholtz equation is separable, then a more detailed cancellation occurs, leaving Q symmetric exactly as was found in the acoustic case.[1]

We sketch the proof for the ellipsoid

$$(x/a)^2+(y/b)^2+(z/c)^2=1 ,$$

which in spherical coordinates may be written schematically

$$[1/r(\theta,\phi)]^2 \doteq 1+\sin^2\theta(1+\cos 2\phi)$$
$$\doteq Y_{e00}+Y_{e02}+Y_{e22} . \qquad (34)$$

First, form the difference

$$Q_{1\sigma mn1\sigma' m'n'} - Q_{1\sigma' m'n'1\sigma mn}$$

from Eq. (31a), with $\sigma+\sigma'$, $m+m'$, $n+n'$ all even by mirror symmetry, Eqs. (32). Considering the last term in the integrand, the radial functions appear in the combination[27]

$$x^2[j_n(x)h_{n'}(x) - j_{n'}(x)h_n(x)] \doteq \sum_{p=0}^{s-1} (1/x)^{2(s-p)-1}, \quad (35)$$

with $n'-n=2s>0$. Now taking the gradient, and employing Eqs. (33) and (34), the radial functions

finally take the form

$$\sum Y_{e|m\pm m'|n''} ,$$

with $0\leq n''\leq n'-n-2$. The corresponding contribution of the spherical harmonics is given by Eq. (33). Because there is no overlap in range of summation, the resulting integral vanishes identically. For the remaining terms in Eq. (31a) one can integrate by parts to remove r_θ, r_ϕ, after using the identity

$$(xj_n)_x(xh_n)_x - x^2 j_n h_n = \tfrac{1}{2}(x^2 j_n h_n)_{xx}$$
$$-\tfrac{1}{2}[n(n+1)+n'(n'+1)]j_n h_{n'} .$$

The analysis now proceeds as before. There is one overlap term in the range of summation this time, but this term constitutes the normal gradient of a potential function and, as discussed above, always vanishes.

For Eq. (31b), the angular functions in the integrand can be written as a scalar product of vector spherical harmonics, but unfortunately the analog of the expansion Eq. (33), for vector harmonics, does not appear to exist in the literature. The symmetry proof can still be carried out, however, by noting from Eq. (34) that

$$(1/x^2)^s \doteq \sum_{0\leq p\leq q\leq s} \cos 2p\phi(\sin\theta)^{2q},$$

then using the identity

$$(2n+1)\sin\theta P_n{}^m = P_{n+1}{}^{m+1} - P_{n-1}{}^{m+1}$$

repeatedly to absorb the factors $\sin\theta$ into the Legendre functions, and finally using orthogonality to complete the proof.

Symmetry of Q does not require choosing an origin at the center of the ellipsoid, and indeed obtains for any origin in the interior. For an origin translated by r_0 from the original, with $R=r-r_0$, the wave functions $\psi(R)$ in the new system are given by[28]

$$\psi(R)=P\psi(r) , \quad \nabla\times\psi(R)=P\nabla\times\psi(r) , \quad R\geq r_0$$

with P a real matrix depending only on r_0. Now from Eq. (10), $Q(r_0)$ in the new system is given by (suppressed index notation)

$$Q(r_0) = \frac{k}{\pi}\int d\boldsymbol{\sigma}\cdot\{[\nabla\times\text{Re}\psi(R)]\times\psi(R)'\}$$

$$= \frac{k}{\pi}\int d\boldsymbol{\sigma}\cdot\{[P\nabla\times\text{Re}\psi(r)]\times\psi(r)'P'\}$$

$$= PQ(0)P' , \qquad (36)$$

and hence is symmetric by inspection.

[26] A. Messiah, *Quantum Mechanics*, translated by J. Potter (Wiley, New York, 1965) p. 1057. In Eq. (33) and subsequently, we use the symbol "$\doteq$" to indicate that only the functions (or additive constants) required on the right-hand side are shown. The explicit expansion coefficients in the sum are not germane, and for simplicity have been omitted.

[27] G. N. Watson, *Theory of Bessel Functions* (Cambridge U. P., Cambridge, England, 1962), 2nd ed., pp. 145–150.

[28] S. Stein, Quart. Appl. Math. **19**, 15 (1961); O. R. Cruzan, *ibid.* **20**, 33 (1962). Because of the restrictions on validity of P, Eq. (36) as derived is only valid for $r_0 \leq \tfrac{1}{2}r_{min}$ on σ, i.e., for an origin translated no more than half the radius of the inscribed sphere of Fig. 1. The process may then be repeated, however, so as to finally locate the origin anywhere in the interior volume.

TABLE I. Form of the matrix elements $Q_{\tau\sigma mn\tau'\sigma'mn'}$ for a rotationally symmetric body (m, n, n' fixed). If in addition there is mirror symmetry normal to the axis of rotational symmetry, then off-diagonal elements also vanish for $(n+n')$ even, diagonal elements vanish for $(n+n')$ odd [Eq. (32c)].

$\tau\sigma$ \ $\tau'\sigma'$	1e	2o	1o	2e
1e	A	B	0	0
2o	B	$(\frac{1}{2}\delta_{nn'}-A)$	0	0
1o	0	0	A	$-B$
2e	0	0	$-B$	$(\frac{1}{2}\delta_{nn'}-A)$

. In consequence of symmetry, the problem is simplified for objects in all 11 coordinate systems in which the scalar Helmholtz equation is separable, computing Q conveniently from

$$Q_{nn'}=Q_{n_> n_<} , \qquad (37)$$

with $n_>$, $n_<$ respectively the greater and lesser of n, n'. Symmetry has been verified directly on the computer for the spheroid and the sphere, the latter with displaced origin. Numerical results are presented below for prolate and oblate spheroids, using Eq. (37).

One final situation remains to be discussed. If the object is rotationally symmetric about the z axis, then $r=r(\theta)$ and there is no coupling between different azimuthal modes, i.e.,

$$Q=0 , \quad m\neq m' . \qquad (38)$$

Using Eqs. (30b), (30c), (32a), and (32b), the form of the matrix elements is shown for fixed n, n' and $m=m'$ in Table I. Note that only two of the sixteen elements are numerically independent. For each fixed m, we can define a reduced matrix, say Q^{rot}, formed from the four elements appearing in the upper left-hand corner of Table I. Again from Table I, Q^{rot} suffices to describe behavior of the (coupled) $\tau\sigma=1e$ and $2o$ modes. Preforming the azimuthal integrations in Eq. (10), we have explicitly

$$Q^{\mathrm{rot}}{}_{(2n-1)(2n'-1)}$$

$$=A=\tfrac{1}{2}(i)\delta_{nn'}-Q^{\mathrm{rot}}{}_{(2n)(2n')}$$

$$=-(\gamma_{mn}\gamma_{mn'})^{1/2}\int_0^{\pi} d\theta \sin\theta$$

$$\times\{[(P_n{}^m)_\theta(P_{n'}{}^m)_\theta+m^2 P_n{}^m P_{n'}{}^m/\sin^2\theta](krj_n)'krh_{n'}$$

$$+P_n{}^m(P_{n'}{}^m)_\theta(kr)_\theta n(n+1)j_n h_{n'}\} , \qquad (39\mathrm{a})$$

$$Q^{\mathrm{rot}}{}_{(2n)(2n'-1)}$$

$$=B=Q^{\mathrm{rot}}{}_{(2n-1)(2n')}$$

$$=-(\gamma_{mn}\gamma_{mn'})^{1/2}m\int_0^{\pi} d\theta(P_n{}^m P_{n'}{}^m)_\theta(kr)^2 j_n h_{n'} . \qquad (39\mathrm{b})$$

The matrix equation for these modes becomes

$$Q^{\mathrm{rot}}T^{\mathrm{rot}}=-\mathrm{Re}Q^{\mathrm{rot}} , \qquad (12')$$

where T^{rot} continues to satisfy the summetry and unitary constraints of Eqs. (21a) and (21b). The real part of Q^{rot} is always symmetric, $Q^{\mathrm{rot}}{}_{n(n+1)}=Q^{\mathrm{rot}}{}_{(n+1)n}$, and of course for quadric surfaces $\mathrm{Im}Q^{\mathrm{rot}}$ becomes symmetric as well.

The remaining elements in Table I describe the modes $\tau\sigma=1o, 2e$, with no coupling to the previous modes. By inspection the Q matrix formed of these elements differs by only a sign change in even rows and columns; the corresponding transition matrix thus has elements given trivially by

$$(-1)^{n+n'}T^{\mathrm{rot}}{}_{nn'} .$$

IV. NUMERICAL RESULTS

The equations have been programmed for solution on the IBM 7030 computer for rotationally symmetric conducting bodies; numerical aspects of the computation are described in detail elsewhere.[29] In brief, matrix elements in Q^{rot} are evaluated using Bode's rule for numerical quadrature.[30] Neumann and Legendre functions are obtained by upward recursion (and Bessel functions by downward recursion), upon specifying the object shape $r(\theta)$ analytically. Results given below for spheroids were obtained by matrix inversion using Eqs. (11) and (27); the cone-sphere and finite cylinder results were obtained by Schmidt orthogonalization using Eq. (28) to compute the transition matrix.

As a check on errors introduced by truncating the infinite system of equations at finite size, a solution can be recomputed using more equations and unknowns, taking relative constancy of the results as a measure of accuracy. Based on this criterion, it was generally found that accuracy of four significant figures or better was achieveable.

Although it is difficult to give an absolute fix on the truncation size adequate for a given object, the following estimates may be helpful, and clearly show the superiority of orthogonalization [Eq. (28)] over matrix inversion [using either Eqs. (11) or Eq. (12), found to be equivalent from the convergence viewpoint]. Define a as the radius of the smallest sphere circumscribing the object, and let N define the truncation, such that Q^{rot} and T^{rot} in Eq. (12') are each $2N$ by $2N$. A convergent solution of Eq. (12') using matrix inversion then generally requires $N/ka\gtrsim 2$, whereas solution by orthogonalization is possible with $N/ka\gtrsim 1$. In view of the $O(N^3)$ operations necessary in either case for each fixed azimuthal mode value m, we conclude that orthogonalization may be up to an order of magnitude faster. Because of their special properties, spheroids constitute an exceptional case for which both methods are equally good, i.e., $N/ka\gtrsim 1$. By way of

[29] P. C. Waterman and C. V. McCarthy, MITRE Technical Paper No. MTP-74, 1968 (unpublished).
[30] Handbook of Mathematical Functions, edited by M. Abramowitz and I. A. Stegun (U. S. Government Printing Office, Washington, D. C., 1964), p. 886.

comparison, the earlier work,[4] which employed outgoing waves to represent surface current, generally required $N/ka \gtrsim 4$. These estimates are all in the "best" case, i.e., objects not drastically different from a sphere. As the object becomes more elongated, for example, N/ka will generally have to be increased.

The prolate spheroid geometry is shown in Fig. 2. The direction of incidence makes an angle u with the axis of rotational symmetry, while the spheroid is characterized by semimajor and semiminor axes a, b respectively (for the oblate spheroid, on the other hand, one has $a < b$). For the incident polarizations $E\|$ and $E\perp$ that are employed, because of rotational symmetry there are no cross-polarized components backscattered.

Consider first the low-frequency Rayleigh limit, for which the backscattering cross section for axial incidence $(u=0)$ is given by[31]

$$\sigma_b/\pi a^2 \approx [2/3M(1-M)]^2 (kb)^4 \qquad (40a)$$

with

$$M \equiv \frac{a^2}{2(a^2-b^2)}\left\{1 - \frac{b^2}{2a(a^2-b^2)^{1/2}}\right.$$

$$\left.\times \ln\left[\frac{a+(a^2-b^2)^{1/2}}{a-(a^2-b^2)^{1/2}}\right]\right\}. \qquad (40b)$$

For the case of a 2:1 prolate spheroid, one obtains

$$\sigma_b/\pi a^2 \approx 0.4724(ka)^4. \qquad (40c)$$

This case was run on the computer with $ka = 0.1$ to obtain the result

$$\sigma_b/\pi a^2 = 0.4691(ka)^4. \qquad (40d)$$

The discrepancy of somewhat less than 1% is probably attributable to the next term of order $(ka)^6$ omitted in the Rayleigh expansion, which would make a correction of order 1% in Eq. (40c).

Moving into the higher ka region, the scattering cross section has been evaluated versus aspect angle for several 2:1 prolate and oblate spheroids, using Eq. (22b). The alternative computation by the forward amplitude theorem, Eq. (22c), was also carried out, and generally found to agree to about seven significant figures. Results are shown in Fig. 3 for incident electric field both parallel and perpendicular to the plane of

Fig. 2. Geometry for scattering by a prolate spheroid, including the two orthogonal incident polarizations.
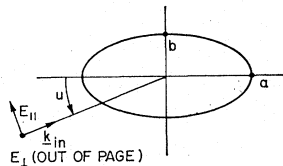
[31] J. W. Strutt (Lord Rayleigh), Phil. Mag. **44**, 28 (1897). See also T. B. A. Senior and P. L. E. Uslenghi, *Electromagnetic and Acoustic Scattering by Simple Shapes*, edited by J. J. Bowman, T. B. A. Senior, and P. L. E. Uslenghi (North-Holland, Amsterdam, 1969), pp. 462–466.
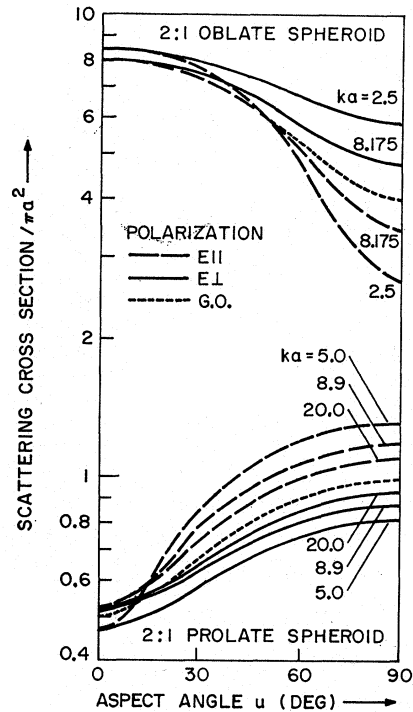

Fig. 3. Computed values are shown for scattering cross section (normalized by πa^2) versus incident aspect angle, for conducting prolate and oblate spheroids with both incident polarizations. For the larger bodies, results are seen to approach the geometrical optics (G.O.) limiting curves.

incidence. It is interesting to note that for all cases shown, as one would probably expect, the total scattering is larger for that polarization having electric vector more nearly parallel to the long dimension of the object.

In the high-frequency geometrical optics limit, the scattering cross section is given simply by twice the area defined by projection of the object onto a plane normal to the direction of incidence.[32] For spheroids one thus gets, after elementary differential-geometry considerations,

$$\sigma_s/\pi a^2 \to 2\times(\text{projected area})/\pi a^2$$

$$= (2b/a)[\sin^2 u + (b/a)^2 \cos^2 u]^{1/2}. \qquad (41)$$

This equation has also been plotted in Fig. 3 (curves labeled G.O.); computed values are seen to approach this limit fairly uniformly with increasing ka.

Backscattering or radar cross section has been evaluated from Eq. (22d). Computed results are shown in Figs. 4–10 for 2:1 prolate spheroids ($ka = 1$, 5, 8.901, 20), a 5:1 prolate spheroid ($ka = 10$), and 2:1 oblate spheroids ($ka = 2.5$, 8.175), respectively. The geometrical optics limit in this case is given by $\pi R_1 R_2$, with R_1 and R_2 the principal radii of curvature at the "specular" point on the object, i.e., that point on the surface having unit normal pointing along the observation

[32] M. Born and E. Wolf, *Principles of Optics* (Pergamon, New York, 1959), p. 656.
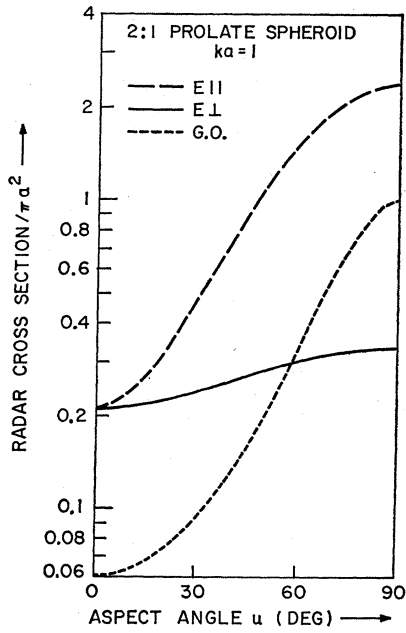
Fig. 4. Computed backscattering or radar cross section shown versus incident aspect angle, for two orthogonal polarizations illuminating a relatively small prolate spheroid. Agreement with the corresponding geometrical-optics prediction is seen to be poor, as would be expected.
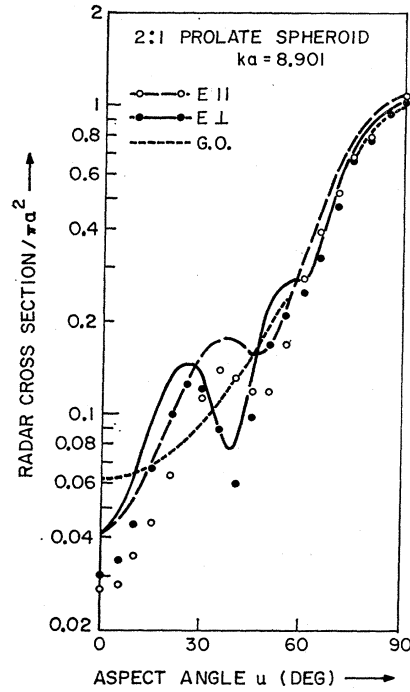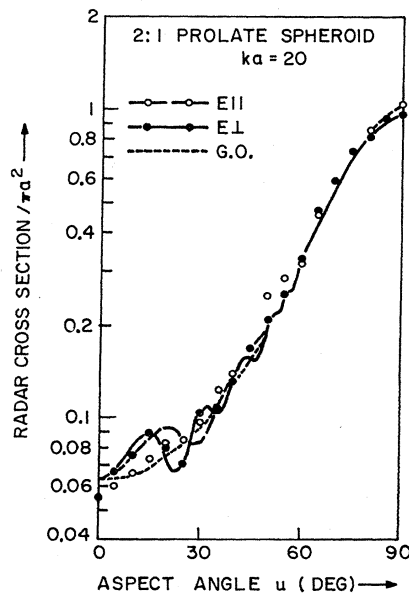

Fig. 6. Theoretical (solid and dashed curves) and experimental (small circles, Ref. 35) radar cross sections are shown versus aspect angle, for a moderately large prolate spheroid. Experimental $E\|$, $E\perp$ shifted down 1.6 dB, 1.0 dB, respectively (see text).
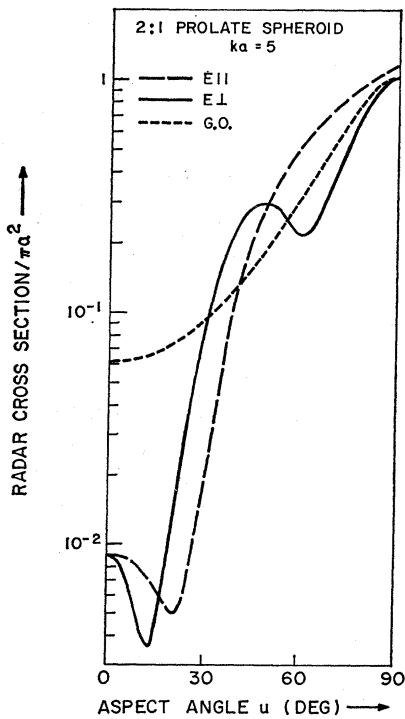
Fig. 5. Computed radar cross section, and the corresponding geometrical-optics limit, are shown as a function of direction of incidence for a prolate spheroid well above the Rayleigh region.

Fig. 7. Theoretical (solid and dashed curves) and experimental (small circles, Ref. 35) radar cross sections are plotted versus aspect angle, for a prolate spheroid with dimensions large compared to wavelength. Agreement with the geometrical-optics limiting value (short dashed curve) is seen to be good. Experimental $E\|$, $E\perp$ shifted up 0.6 dB, down 0.3 dB, respectively.
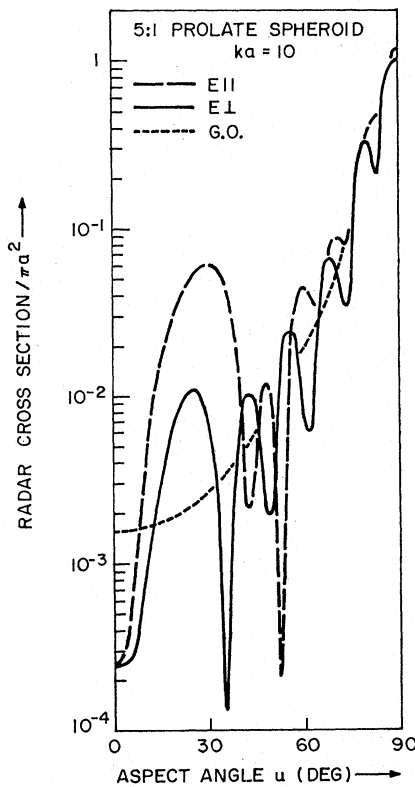
FIG. 8. Theoretical radar cross section plotted as a function of aspect angle for a 5:1 prolate spheroid. Here the semimajor and semiminor axes are respectively greater and less than wavelength.
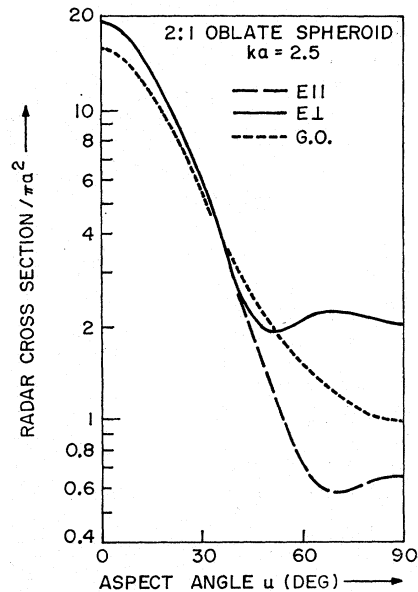

FIG. 9. Computed radar cross section shown versus aspect angle for a 2:1 oblate spheroid with both axes somewhat less than wavelength. For this case, set $b=2a$ in Fig. 2.

direction. In particular, for spheroids one obtains[38]

$$\sigma_b/\pi a^2 \to 1/[\sin^2 u + (a/b)^2 \cos^2 u]^2 . \qquad (42)$$

Curves obtained from Eq. (42) are shown in Figs. 4–10, and one observes that agreement of the computed results with the geometrical-optics limit improves both with increasing ka and at aspects for which the appropriate radii of curvature are both large compared with wavelength. The latter effect is seen clearly for the oblate spheroids (Figs. 9 and 10) at aspect angles near end-on (i.e., u not too close to 90°). Note also the relatively large fluctuations in radar cross section associated with the 5:1 prolate spheroid of Fig. 8. The geometrical optics approximation fails even in order of magnitude to represent a peak in the vicinity of $u=30°$. High-frequency approximations are of course not appropriate in this instance; although the semimajor axis is somewhat greater than the wavelength, the semiminor axis is not (i.e., $b=\lambda/\pi$).

An independent check exists for the computed curves of Fig. 6. This case, the 2:1 prolate spheroid with $ka=8.901$, has been evaluated by Andreasen by numerical solution of the integral equation for induced

surface current.[34] The theoretical procedure used was altogether different from ours; the resulting curves for radar cross section are graphically indistinguishable from those of Fig. 6. (Closer examination reveals numerical agreement between the two computed results within 0.1 dB.[34])
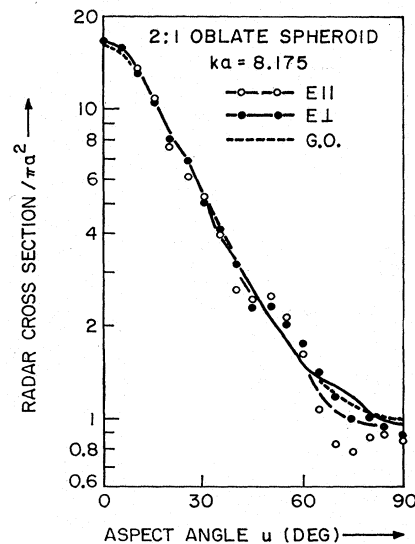

FIG. 10. Theoretical (solid and dashed curves) and experimental (small circles, Ref. 35) radar cross sections are plotted versus aspect angle for a 2:1 oblate spheroid. Both semiaxes are larger than wavelength, and excellent agreement is seen to obtain with the geometrical-optics limit (short dashed curve). Experimental $E\perp$ shifted up 0.6 dB, $E\|$ unshifted (see text).

[38] J. E. Burke and V. Twersky, J. Acoust. Soc. Am. **38**, 589 (1965).

[34] M. G. Andreasen, IEEE Trans. Antennas and Propagation **13**, 303 (1965); **14**, 659 (1966). This author has also discussed two-dimensional problems, in IEEE Trans. Antennas and Propagation **12**, 746 (1964).
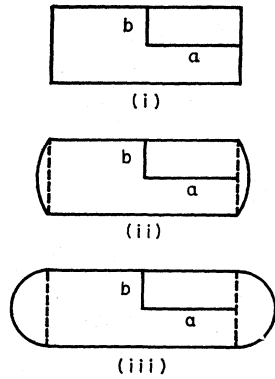
FIG. 11. A cross-section view of three finite cylinders chosen to test the theory in the presence of edges: (i) right circular cylinder, (ii) finite circular cylinder with spherical endcaps (sphere radius equals twice cylinder radius), (iii) smooth circular cylinder with hemispherical end caps.

Experimental measurements of radar cross section were made for two of the prolate spheroids, and the larger oblate spheroid; resulting values are shown by the small circles in Figs. 6, 7, and 10. The models themselves, including also the finite cylinders described below, were machined at MITRE from solid aluminum stock, holding a tolerance of about 0.001 in. Microwave scattering measurements were then performed at the RCA laboratories in Moorestown, N. J., at a frequency of 9.930 GHz ($\lambda = 3.019$ cm), using for calibration a secondary standard consisting of a finite cylinder of known broadside radar cross section.[35]

Slight inconsistencies were apparent in the measurements themselves (e.g., different experimental values

for the two polarizations at end-on incidence, $u = 0$, when theoretically they should be identical by symmetry). Because of this, we have decided for clarity to shift the experimental results so as to match theory and experiment at the peak value of radar cross section, where both should be most accurate. In these instances, the amount of shift, in dB, is noted in the figure captions. The resulting agreement between theory and experiment for spheroids is seen to be reasonably good, the worst discrepancy of about 1 dB occurring with the smaller prolate spheroid of Fig. 6.

Consider next the finite cylinders shown (in section) in Fig. 11. Dimensions for the right circular cylinder are shown in Fig. 11(i). Keeping the basic dimensions fixed, the shape is then modified to the finite cylinder of Fig. 11(ii) by adding spherically bounded ends, with radii of curvature equal to twice the cylinder radius b. Finally, the smooth finite cylinder of Fig. 11(iii) is obtained by adding hemispherical ends (radii of curvature equal to cylinder radius).

The cylinders were evaluated for 60 aspect angles in the interval $0° \le u \le 90°$, using Schmidt orthogonalization to first compute the transition matrix from Eq. (28) in terms of Q^{rot}. Values obtained for radar cross section are shown as small circles in Figs. 12 and 13 for the two cylinders having edges. Experimentally measured values[35] are shown by the solid lines. Agreement between theory and experiment is seen to be
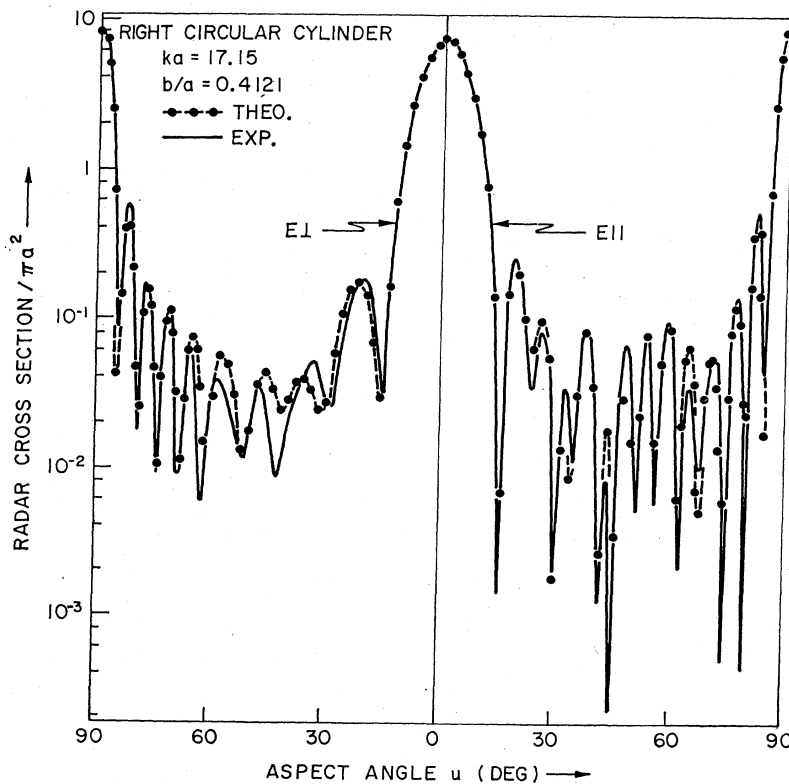

FIG. 12. Theoretical and experimental (Ref. 35) radar cross sections are shown versus aspect angle for the right circular cylinder of Fig. 11 (i). Lobe structure near broadside ($u = 0$ deg) and end-on ($u = 90$ deg) incidence is quite accurately predicted by the physical optics approximation. Experimental $E\|$, $E\bot$ shifted up 1.2 dB, 1.9 dB, respectively (see text).

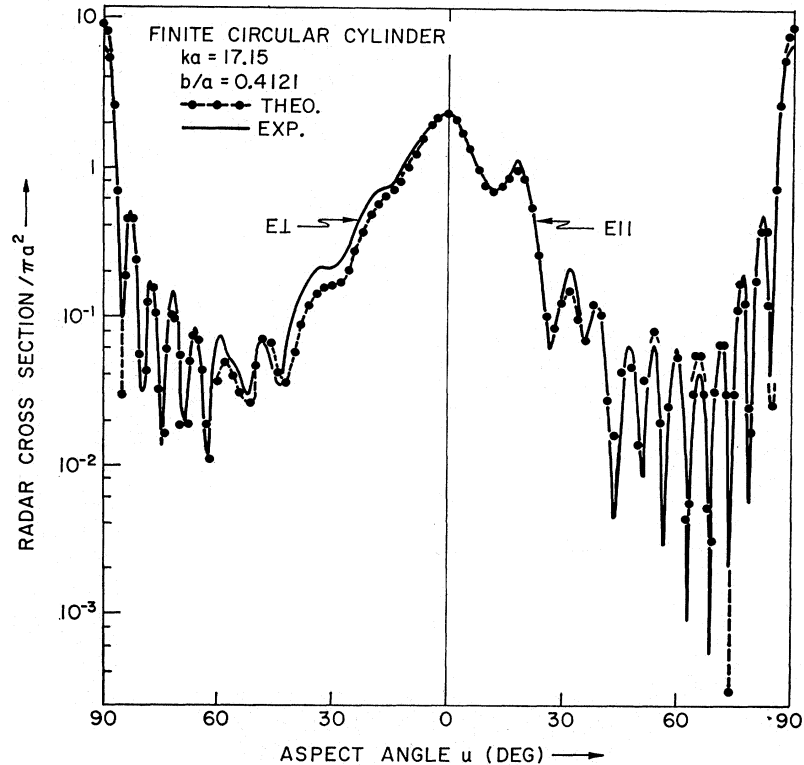[35] D. P. Malloy and H. Spiegel (private communication).

FIG. 13. Theoretical and experimental (Ref. 35) radar cross sections are plotted as a function of aspect angle for the finite circular cylinder of Fig. 11(ii). Whereas the return near broadside ($u=90°$) is virtually unchanged from that of the right circular cylinder (Fig. 12), the return in the vicinity of end-on incidence ($u=0$ deg) is radically different, and strongly dependent on polarization. Experimental measurements have been shifted up 0.2 dB for both polarizations (see text).

remarkably good, especially when one notes that the scale of the figures in each case encompasses about five orders of magnitude.

The sharp lobe structure seen in the figures in the vicinity of broadside ($u=90°$) for both cylinders can be fit fairly well by the physical-optics approximation (Kirchhoff approximation for surface field), which gives[36]

$$\sigma/\pi a^2 \approx b \; \sin u \; \sin^2(2ka \; \cos u)/\pi ka^2 \cos^2 u. \quad (43)$$

Similarly for near-axial incidence ($u=0°$), the main lobe exhibited in the radar cross section of the right circular cylinder, Fig. 12, is describable by the approximate formula[36]

$$\sigma/\pi a^2 \approx (b/a)^2 \; \cot^2 u J_1^2 (2kb \; \sin u) \quad (44)$$

(J_1=Bessel function) for backscattering by circular plates. Such is not the case for near-axial incidence on the finite cylinder of Fig. 13, however; a more sophisticated approach would be required, capable of disting-uishing between the two incident polarizations.

A similar computation was attempted for the smooth, finite cylinder of Fig. 11(iii), after increasing matrix size slightly to allow for the increased over-all cylinder length.[37] Rather to our surprise, in view of the fact that this was the only cylinder considered *without* edges, no agreement with experiment was achieved,

and we conclude that the computation failed in this instance. Failure is tentatively ascribed to the numerical quadratures used to obtain elements of Q^{rot}; we defer comment until after the next example, where the same situation recurs.

The final case of interest consists of a 15° half-angle cone, joined smoothly to a sphere of radius a. The geometry is shown in Fig. 14. For this case the object does not possess mirror symmetry normal to the rotational symmetry axis, and scattered field quantities must be evaluated over the full range of aspects $0° \leq u \leq 180°$.

Measurements for the cone-sphere were made on the microwave scattering range at Avco Corporation, Wilmington, Mass.[38] Again using a target machined out of aluminum, continuous backscattering measurements were made over the full 360° range of aspects for each polarization, at a frequency of 34.25 GHz ($ka = 3.66$). Discrepancies between the two 180° passes, shown by the two light curves in Figs. 15 and 16 for

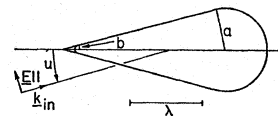

FIG. 14. Geometry of a smoothly joined cone-sphere is shown. For the computations, the cone tip was rounded off to a radius $b=0.1a$, changing the dimensions negligibly in comparison with wavelength, as can be seen.

---

[36] J. R. Mentzer, *Scattering and Diffraction of Radio Waves* (Pergamon, London, 1955) pp. 108 and 131.

[37] Truncation at $N=24$, 26, 28 was used for the three cylinders of Fig. 11, respectively.
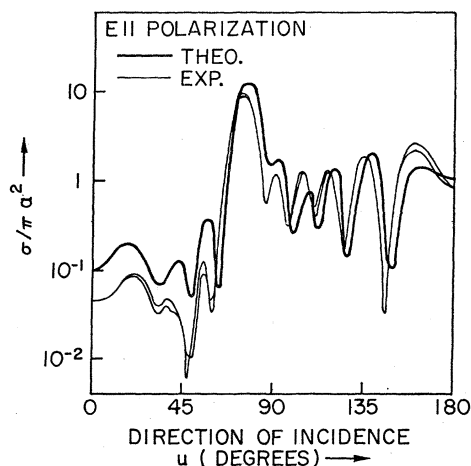
[38] N. E. Pedersen (private communication).

FIG. 15. Theoretical (heavy curve) and experimental (light curves, Ref. 38) radar cross sections of the cone-sphere plotted versus aspect angle over the full range $0 \le u \le 180$ deg for $E \parallel$ polarization. The large peak at $u \simeq 75$ deg is due to a specular "glint" from the cone section.

each of the polarizations, give a measure of experimental error, which is seen to be extremely good, almost without exception in the range $\pm \frac{1}{2}$ dB. The calibration target was an aluminum sphere of known radar cross section.

The first attempt at computation, using Schmidt orthogonalization, again failed. This time, however, the trouble could be traced to the numerical quadratures used to obtain elements of Q^{rot} from Eqs. (39). Values obtained for many of the elements refused to settle down, with decreasing step size, beyond two or three significant figures (as contrasted with eight or ten significant figures usually readily achievable).

The computation was then modified by rounding off the cone tip to a spherical radius $b = 0.1a$. As can be seen from Fig. 14, the resulting dimensional changes
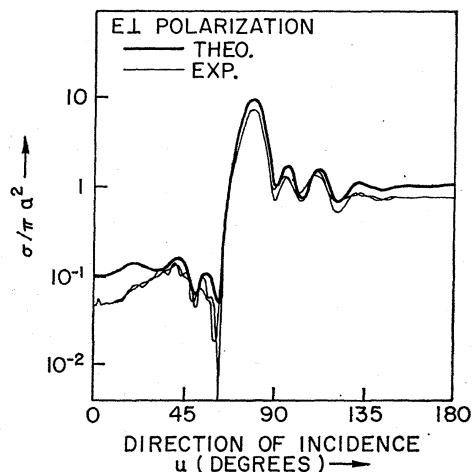

FIG. 16. Theoretical (heavy curve) and experimental (light curves, Ref. 38) radar cross sections of the cone-sphere shown as in Fig. 15, but for $E \perp$ polarization. Curves for the two polarizations differ considerably, except for the specular glint at $u \simeq 75°$, which is virtually unchanged.

are quite small in comparison with wavelength. The coordinate origin was also shifted to the right, so as to remain centered on the long dimension of the (sphere) cone-sphere. Slightly better convergence was obtained, resulting in the heavy curves shown in the figures. Good correlation is seen between theory and experiment for both number and location of peaks, with numerical agreement generally good to within 3 dB.

Computational difficulties encountered with the cone-sphere, as well as the finite cylinder of Fig. 11(iii), can now be explained as follows: In numerically integrating *over the spherical portion only* of the cone-sphere, the function $r(\theta)$ appearing in the integrand becomes singular at an angle slightly beyond the upper end point of integration (that point where the radius vector is tangent to the continuation of the sphere). Consequently the error term in Bode's rule, which is proportional to the sixth derivative of the integrand,[30] although not infinite can become extremely large. Shifting of the origin, in the course of rounding off the cone tip, served to move the singularity slightly further beyond the range of integration, alleviating the difficulty just enough that results could be obtained. Note that exactly the same situation arises with the smooth cylinder (but not the other two cylinders) of Fig. 11. Although we have not attempted to do so, it would appear that these numerical quadrature difficulties could be avoided completely by changing over to integration with respect to arc length in Eqs. (39).

Some comment on the computer runs is of interest. The cone-sphere results shown in Figs. 15 and 16 required about $5\frac{1}{2}$ min of computer time. The first seven azimuthal modes ($0 \le m \le 6$) were employed, in each case truncating at $N = 14$, or a full matrix size of 28×28 complex.[39]

For larger bodies, computation time increases roughly proportional to $(ka)^4$; of this, one factor $N^2 \simeq (ka)^2$ is due to the number of matrix elements of Q^{rot} required, another factor proportional to ka arises from the number of points employed in numerical quadrature, a final factor, also proportional to ka, accounts for the number of azimuthal modes which must be included. Experience indicates that the subsequent arithmetic operations involved in matrix processing (inversion or orthogonalization, multiplication), which are also $O(ka)^4$, represent an insignificant fraction of the total computation time. Mirror symmetry (e.g., the finite cylinders) reduces the computation by a factor of 4; half of the elements of Q^{rot} vanish, the remainder may be evaluated by integrating over the reduced range $0 \le \theta \le \frac{1}{2}\pi$ in Eqs. (39). A further reduction of 33% obtains for spheroids, because elements of $\text{Im} Q^{\text{rot}}$ above the diagonal need not be evaluated.

[39] In the absence of numerical quadrature difficulties, we estimate that $N \simeq 10$, and perhaps 50 integration intervals, rather than the abnormally large 500 intervals actually used, would have sufficed. If so, computation time would be reduced by a factor of about 20.

V. DISCUSSION

Some of the basic features underlying a matrix formulation of electromagnetic scattering have been presented, together with sufficient numerical results to suggest that the method is ideally suited for digital computation for bodies with and without edges, especially if quadrature problems can be resolved. As has already been noted in the Introduction, the present work is closely interwined with an earlier paper giving the scalar formulation for acoustic scattering.[1] The reader is advised to look therein for a more detailed discussion of eigenfunctions and their application, and a completeness proof for regular wave functions restricted to a surface. By the same token, the result that symmetry of Q, for quadric surfaces, is invariant to coordinate translation, and the approach using Schmidt orthogonalization, apply also in the scalar case, *without change of notation.*

The main unfinished business in the theory is concerned with rigorous convergence proofs, and consequent error bounds, associated with truncation of infinite-dimensional matrices. Although some empirical error bounds have been noted in the discussion of numerical results, the convergence question is clearly far from fully answered.[40]

In conclusion, several additional research questions come to mind, as follows.

1. The surface currents, which were eliminated from the equations in the present work, are nevertheless of interest in their own right. They may be obtained from Eqs. (9) and (11b), using expansion coefficients

$$\alpha = -i(Q')^{-1}a ,$$

or perhaps more conveniently in consequence of Eq. (26),

$$\alpha = -iM'\hat{Q}^* .$$

Results would appropriately be compared with the work of Andreasen,[34] in which surface currents are the primary unknown. Bodies with edges (e.g., the finite cylinders of Fig. 11) are of special interest; it would be instructive to examine in detail the manner in which the expansion of Eq. (9) approximates the nonanalytic behavior of the surface currents known to arise in the vicinity of edges.

2. The matrix $P(\mathbf{r}_0)$, which served to reexpress the spherical wave functions about a new origin, maps one orthonormal basis onto another. Consequently P must

be orthogonal, and Eq. (36) may be rewritten as

$$Q(\mathbf{r}_0)P(\mathbf{r}_0) = P(\mathbf{r}_0)Q(0) .$$

In particular, if Q is defined for a spherical surface of radius $a > 2r_0$, centered about the original origin, then $Q(0) \equiv \Lambda_a$ is diagonal with explicitly known elements, while $Q(\mathbf{r}_0) \equiv Q_a$ is a symmetric matrix defined by Eqs. (10) and (37), and

$$Q_a P(\mathbf{r}_0) = P(\mathbf{r}_0)\Lambda_a .$$

That is to say, *the columns of P are eigenvectors of Q_a having known eigenvalues* (entries of Λ_a). Furthermore, P is real, and both the real and imaginary parts of the above equation must hold separately. This definition of P in terms of an eigenvalue problem is quite unrelated to the earlier procedure in the literature[28]; comparison of the two approaches would be of theoretical interest, and might well give new insight to the structure of P.

3. In the low-frequency limit, terms in the Rayleigh expansion may be obtained systematically from Q for both conducting and dielectric ellipsoids, following a procedure outlined in the acoustic case.[1] It would be of interest to carry out these calculations, making comparison with the work of Stevenson.[41]

4. It should be possible to obtain the Q matrix for a conducting elliptic disk as a limiting case of the oblate ellipsoid, in close analogy to the earlier treatment of the strip as the limit of an elliptic cylinder.[1] Vector eigenfunctions of the disc could then be defined, and compared with the classic work of Meixner and Andrejewski for the special case of the circular disk.[42]

5. For plane-wave incidence along the symmetry axis of a conducting paraboloid of revolution, Schensted has shown that the geometrical optics approximation in fact constitutes the exact, closed form solution for the scattering.[43] Study should confirm that this result follows also in the present context. Schensted's work was carried out in a geometrical optics framework, and restricted to axial incidence in order that no shadow boundaries be present on the paraboloid. Such a constraint is quite irrelevant to us, however. Thus, knowing a solution for axial incidence, it may be possible to infer a solution for general direction of incidence.

[40] We expect, because of symmetry of Q [Eq. (37)] and the behavior of the spherical Bessel and Neumann functions for index large compared with argument, that the convergence question is easily resolvable for ellipsoids. Indeed, for both scalar and vector problems concerned with ellipsoids, including cases where standard separation of variables techniques can also be used, the present method may well be optimum whenever hard numerical results are desired. This comment is based on the fact that only in spherical (or circular cylindrical) coordinates are there simple recursion relations for generating the wave-functions.

[41] A. F. Stevenson, J. Appl. Phys. **24**, 1134 (1953); **24**, 1143 (1953). See also Senior and Uslenghi, Ref. 31.
[42] J. Meixner and W. Andrejewski, Ann. Physik **7**, 157 (1950); W. Andrejewski, Z. Angew. Phys. **5**, 178 (1953).
[43] C. E. Schensted, J. Appl. Phys. **26**, 306 (1955).